Few-layer MoS_2 saturable absorbers for short-pulse laser technology: current status and future perspectives [Invited]

R. I. Woodward,[1,*] R. C. T. Howe,[2] G. Hu,[2] F. Torrisi,[2] M. Zhang,[1] T. Hasan,[2] and E. J. R. Kelleher[1]

[1]*Femtosecond Optics Group, Department of Physics, Imperial College London, SW7 2AZ, UK*
[2]*Cambridge Graphene Centre, University of Cambridge, Cambridge, CB3 0FA, UK*
**Corresponding author: r.woodward12@imperial.ac.uk*

Received January 6, 2015; accepted February 1, 2015;
posted February 11, 2015 (Doc. ID 231538); published March 24, 2015

Few-layer molybdenum disulfide (MoS_2) is emerging as a promising quasi-two-dimensional material for photonics and optoelectronics, further extending the library of suitable layered nanomaterials with exceptional optical properties for use in saturable absorber devices that enable short-pulse generation in laser systems. In this work, we catalog and review the nonlinear optical properties of few-layer MoS_2, summarize recent progress in processing and integration into saturable absorber devices, and comment on the current status and future perspectives of MoS_2-based pulsed lasers.

OCIS codes: (140.3538) Lasers, pulsed; (160.4236) Nanomaterials; (160.4330) Nonlinear optical materials; (230.4320) Nonlinear optical devices.
http://dx.doi.org/10.1364/PRJ.3.000A30

1. INTRODUCTION

Short-pulse lasers are becoming ubiquitous tools in a wide variety of applications, including industrial materials processing, biomedical imaging, and fundamental research [1–4]. This is driven by advances in saturable absorber (SA) technologies, in addition to new gain media [5,6], enabling more versatile pulse sources. A SA acts as a passive optical switch in a laser cavity to enable short-pulse generation by passive mode-locking or Q switching [1]. The currently dominant SA technologies, such as semiconductor SA mirrors (SESAMs) and nonlinear polarization evolution (NPE) possess limitations—for example, SESAMs typically exhibit narrowband operation and limited (~picosecond) response times without post-processing [7,8] and NPE is highly sensitive to environmental fluctuations [9]—driving research to consider alternative materials with nonlinear optical properties for SAs and other novel photonic devices.

Intense research into the field of low-dimensional nanomaterials has recently demonstrated that one-dimensional (1D) and quasi-1D nanomaterials, such as single- and multi-wall carbon nanotubes formed of single or few atomic layer thick tubes of atoms respectively [10,11], and two-dimensional (2D) and quasi-2D nanomaterials, such as mono- and few-layer graphene [12,13] consisting of single or few layers of atoms, exhibit remarkable optical and electrical properties and environmental robustness [11,13]. This suggests their suitability as candidate materials for the development of future photonic technologies [11,13]. While carbon nanotubes [14,15] and graphene [16,17] have emerged as promising materials for SA devices, as well as a more general platform for novel optoelectronic systems [11,13], they are only two examples of a wider class of nanomaterials that are currently being investigated, including few-layer transition-metal dichalcogenides (TMDs) [18] and quasi-2D materials such as Bi_2Te_3 and Bi_2Se_3, which are topological insulators in their bulk form [19]. These other nanomaterials offer distinct yet complementary properties to carbon nanotubes and graphene [18,19].

TMDs are layered materials with an MX_2 stoichiometry [20]. Each layer consists of a single plane of hexagonally arranged transition metal (M) atoms (e.g., Mo, W) held between two hexagonal planes of chalcogen (X) atoms (e.g., S, Se) by strong covalent bonds [Fig. 1(a)] [20]. Depending on the coordination and oxidation states of the transition metal atoms, TMDs can either be semiconducting or metallic in nature [18]. In bulk form, individual MX_2 layers are held together by relatively weak van der Waals forces [20], which have enabled monolayer (2D) and few-layer (quasi-2D) flakes of TMDs to be exfoliated. The optical and electronic properties of such flakes has been found to be strongly thickness-dependent, with monolayer and bulk forms possessing distinct properties [18]. Recently molybdenum disulphide (MoS_2), a TMD, has received particular attention due to its layer-dependent optoelectronic properties [21]. In bulk form, MoS_2 has an indirect 1.29 eV (961 nm) bandgap, whereas monolayer MoS_2 is a non-centrosymmetric material with a direct 1.80 eV (689 nm) energy gap [22]. Contemporary studies have highlighted the favorable optoelectronic properties of monolayer and few-layer MoS_2, including strong photoluminescence in monolayers [23], current on/off ratios exceeding 10^8 in field-effect transistors [24], and a nonlinear optical response stronger than that of graphene [25], paving the way for the development of new photonic devices such as SAs for pulsed laser technology.

Reports of few-layer MoS_2 and observations of their thickness-dependent properties first appeared in the literature many decades before the graphene-led renaissance in 2D

materials [26]. In 1963, Frindt and Yoffe studied the optical properties of thin (<10 nm thick) MoS_2 crystals, later identifying new features in the absorption spectrum of few-layer MoS_2 flakes (mechanically exfoliated with adhesive tape) [27–29]. Reports of monolayer exfoliation using lithium-based intercalation techniques were also published [30]. However, early studies were limited by the instrumentation and techniques available for characterization that would not meet today's standards for imaging single and few atomic layers; neither the nonlinear optical properties of few-layer MoS_2 nor the technological benefits were exploited.

In this review, we consider the current state of few-layer MoS_2-based photonics, with a particular focus on fabrication techniques, integration strategies, and nonlinear optical properties and applications. We catalog the properties of MoS_2 SA devices and the performance parameters of MoS_2-based short-pulse lasers to date. It is concluded that few-layer MoS_2 could play a significant role in future optoelectronic and photonic technologies, particularly as a wideband SA for versatile pulsed laser sources.

2. PROCESSING AND DEVICE INTEGRATION

A variety of techniques exist for producing mono- and few-layer MoS_2 flakes, complemented by a range of flexible integration platforms for including flakes in practical devices for target applications [18]. To commercially exploit such devices, modern manufacturing techniques are required for large-scale, low-cost fabrication of few-layer materials [31].

In this section, we briefly consider the processing of MoS_2 flakes, the characterization techniques available to quantify flake morphology and number of layers, and the integration platforms used for the development of SA devices. We conclude with a fabrication case study, outlining the steps involved in the production of few-layer MoS_2–polyvinyl alcohol (PVA) composite films.

A. Monolayer and Few-Layer MoS_2 Fabrication

Few-layer fabrication techniques can be broadly separated into two approaches [18,31,32]: top-down exfoliation (including mechanical cleavage and solution-processing techniques) and bottom-up growth (such as chemical vapor deposition (CVD) and pulsed laser deposition (PLD)). It should be noted that there is no standardized agreement in literature for the number of MoS_2 layers required for classification as "few-layer MoS_2" compared to bulk MoS_2. In the graphene community, few-layer graphene is generally accepted to consist of fewer than 10 monolayers [26]; however, in this review, we include reports in the literature of few-layer MoS_2 with up to 30 layers (~20 nm).

Mechanical exfoliation involves repeatedly cleaving layers from bulk layered crystal materials, often using adhesive tape, leaving few-layer and a small number of monolayer flakes [18,33]. This was the first reported technique for obtaining few-layer flakes of MoS_2 [28], and can be used to produce high-quality, single-crystal flakes [33]. However, despite widespread usage of the mechanical cleavage technique for fundamental studies of 2D materials [23,33,34], poor scalability and low yield render it unsuitable for realistic large-scale applications.

CVD offers a scalable method for the production of single- and few-layer MoS_2 [35,36]. For example, solid precursors MoO_3 and sulfur are heated in a furnace to ~650°C [37]. The sulfur vapor reduces the MoO_3, first forming volatile MoO_{3-x} compounds before being catalyzed by the substrate to form a single- or few-layer film of MoS_2 [37–40]. The film growth is limited by the low nucleation rate on bare substrates, and pretreatment of the substrate is often necessary to seed the MoS_2 growth [40].

Another growth technique is hydrothermal synthesis, where crystallization is achieved at a high vapor pressure reaction and elevated temperatures. In [41], few-layer MoS_2 flakes were fabricated by a hydrothermal reaction between sodium molybdate ($NaMoO_4$) and silicotungstic acid ($H_4[W_{12}SiO_{40}]$) at 240°C for 24 h with thiourea as the sulfurization reagent. However, the mechanism for the formation of the nanosheets from the reaction, which typically produces 1D structures, is not explained.

PLD produces films of material following ablation from a target, such as bulk MoS_2 crystals [42,43]. The target is placed in a chamber (typically under vacuum) and irradiated, producing a plume of ejecta which can be deposited onto a substrate. In particular, the technique allows control over the ratio of molybdenum to sulfur in the film due to the different evaporation rates of the two ions [43].

Solution processing of MoS_2 is a widely used technique that produces a high yield of mono- and few-layer flakes dispersed in liquid, carried out under ambient conditions with a high throughput [31]. MoS_2 can either be chemically exfoliated (e.g., via lithium intercalation) [30,44,45] or dispersed into select solvents via liquid phase exfoliation (LPE) [46].

Chemical exfoliation of MoS_2 is typically achieved via lithium intercalation followed by hydrothermal exfoliation [30,44,45,47–49]. The intercalant increases the separation between MoS_2 layers, allowing exfoliation into solvents via stirring or ultrasonication [30,44,45]. The use of lithium compounds as an intercalant enhances the process via the release of hydrogen on exposure to water [30]. However, exfoliation of MoS_2 by this method can lead to structural alterations in the material [44,50], producing the 1T MoS_2 phase, and requiring annealing at ~300°C to restore the 2H phase of untreated MoS_2 [44]. The 2H and 1T phases of MoS_2 differ in the coordination of the Mo atoms, which is trigonal prismatic in the 2H phase and octahedral in the 1T phase [44,50,51]. Unlike 2H-MoS_2, 1T-MoS_2 is metallic due to degeneracies in the band structure [52]. The presence of 1T-MoS_2 in intercalated samples is evidenced by the absence of photoluminescence, even in monolayer flakes [44], as well as by differences in the Raman and optical absorption spectra [44].

LPE involves three main steps: (1) dispersion of bulk MoS_2 in a solvent, (2) exfoliation, and (3) purification [32]. First, bulk MoS_2 is dispersed in a suitable solvent (one that minimizes the interfacial tension between the liquid and material [53]). Ultrasound-assisted exfoliation is then used to exfoliate few-layer MoS_2 flakes from the bulk by cavitational waves (from the formation, growth, and collapse of bubbles and voids in the liquid due to pressure fluctuations [54]). Finally, exfoliated few-layer flakes are separated from unexfoliated thick flakes, usually through ultracentrifugation. Ultracentrifugation also enables sorting of MoS_2 flakes by thickness, providing a route to engineering MoS_2 dispersions with desired flake sizes [55].

Finally, we note that other few-layer MoS_2 fabrication techniques exist such as physical vapor deposition [40] and gas

phase growth [56], although here we have restricted the scope of our review to those which, to date, have been used to produce SA devices.

B. Material Characterization

1. Raman Spectroscopy

Raman spectroscopy is a very popular tool to study crystal quality [34,57], as well as accurately determine the number of layers in MoS_2 flakes [57]. MoS_2 has four Raman-active modes (E_{1g}, E^1_{2g}, A_{1g}, and E^2_{2g}) and two IR-active modes (A_{2u} and E_{1u}) [58,59]. The E^1_{2g} is an in-plane mode generated by the opposing vibration of the two S atoms with respect to the Mo atom, while the A_{1g} mode comes from the out-of-plane modes of S atoms vibrating in opposite directions. From monolayer to bulk, the E^1_{2g} mode redshifts [57,59]. This has been attributed to an enhancement of the dielectric screening of the long-range Coulomb interaction between the effective charges with a growing number of layers [59]. On the other hand, the A_{1g} mode blueshifts, which has been attributed to increased van der Waals interactions in thicker samples [60,61]. The frequency shift between E^1_{2g} and A_{1g} modes is often used to determine the number of layers [57]. Several other Raman-active modes have been identified at low frequency (around 7 and 25 cm^{-1}) for multilayer MoS_2 flakes [62]. In single-layer MoS_2, there are no rigid-layer vibrations [62]. For multilayer MoS_2, these have been grouped into shear modes (C) and layer breathing modes (LBMs). C modes redshift while LBMs blueshift with increasing number of layers [62]. It is, however, important to note that there are multiple factors affecting the different Raman modes active in MoS_2 (interlayer coupling, coulomb interaction, breathing modes, adsorbates, doping, etc.), making it impossible to generate a complete interpretation of the Raman spectrum of MoS_2.

2. Transmission Electron Microscopy

Standard bright field transmission electron microscopy (TEM) can be used to estimate the length and width of the flake [46,63]. High-resolution TEM (HRTEM) can be used to identify single layers and estimate the number of layers in few-layer samples. Analysis of the intensity profile of the HRTEM micrographs for single-layer MoS_2 reported a difference between the intensity peaks corresponding to the two neighboring Mo and S atoms. The intensity ratio has been estimated to be 1.15 for single-layer MoS_2. Such an intensity difference has been reported for very low odd number of layers, with the effect being less evident with increasing number of layers. On the other hand, no difference between the intensity peak corresponding to neighboring atoms has been reported for a MoS_2 flake with an even number of layers, because of the evenly repeated ABAB stacking sequence of MoS_2 layers [46].

C. Integration Schemes

There are numerous platforms for integrating few-layer MoS_2 flakes with standard optical components or substrates to form SA devices, depending on the technique used to process the flakes.

Solution-processed dispersions of few-layer MoS_2 flakes have been integrated into SA devices by coating [48,49,64–69] or transfer of filtered films [46,70] onto substrates such as fiber facets, or by blending with polymers to produce freestanding composites [47,71–75], similar to integration techniques employed for LPE graphene flakes [15]. Additionally, mechanically exfoliated few-layer MoS_2 flakes can be integrated in similar ways if the exfoliated flakes are dispersed in a solvent [76], although the process was not fully described. A widely used technique to form a flexible and freestanding SA device which can be sandwiched between two fiber patchcords in a fiber laser is to embed few-layer MoS_2 flakes in a PVA polymer film [47,71–75]. Polymeric materials are an ideal choice of platform to integrate nanomaterials into photonic systems, as they are easily manipulated by methods such as embossing, stamping, and etching, and generally have a low-cost, room-temperature fabrication process [15]. However, thermal damage of the polymer can limit their use in high-power fiber and bulk lasers. To circumvent this, few-layer MoS_2 flakes can be directly deposited on a fiber facet by optically driven deposition from a LPE dispersion [66] or spin-coated onto quartz [66] or BK7 glass [69]. Another integration strategy, which increases the interaction length between light and MoS_2, is to deposit few-layer MoS_2 dispersion along a microfiber [48,49] or side-polished fiber [76], causing the SA to interact with the evanescent optical field.

Few-layer MoS_2 is typically grown by CVD on Si/SiO_2 or sapphire [77]. Integration of such MoS_2 flakes to form SA devices requires flake transferring and placement techniques to move flakes to a desired photonic substrate [38–40]. PLD-fabricated MoS_2 flakes require a similar transfer technique, or alternatively, the desired substrate can be used directly in the PLD process [42]. For flake transfer, a polymer such as polymethyl methacrylate is generally spin-coated onto the MoS_2 as-grown film [38,40]. The growth substrate is etched (for example, with hydrofluoric acid [40,77] or potassium hydroxide [40,78]) to lift off the polymer–MoS_2 film, which can then be rinsed and transferred to the new substrate. Finally, the polymer layer is dissolved, leaving the MoS_2 film on the substrate [38–40]. This approach has been used for transferring few-layer MoS_2 films directly onto a fiber connector [77,79] and for exploiting evanescent field interaction by depositing CVD-grown MoS_2 on a side-polished fiber [78].

D. Few-Layer MoS_2–PVA Composite SA: A Fabrication Case Study

Here, we illustrate the fabrication procedure of a few-layer MoS_2–PVA composite SA device by briefly outlining our typical experimental procedure using LPE. This type of SA has been successfully used for laser pulse generation, continuously tunable within the ranges 1030–1070 [72] and 1535–1565 nm [73].

First, MoS_2 powder (120 mg) is mixed with 90 mg of sodium deoxycholate bile salt in 10 mL of deionized water for ultrasonication (~2 h) at a constant temperature of ~5°C. The thick unexfoliated bulk MoS_2 flakes are sedimented via ultracentrifugation (4200 *g*), and the top 80% of the dispersion, enriched in single- and few-layer flakes, is collected.

The absorption spectrum of this dispersion, diluted to 10 vol %, is shown in Fig. 1(b). The four observed peaks, at ~665, ~605, ~440, and ~395 nm, are termed A, B, C, and D according to standard nomenclature [20], and result from excitonic transitions (A,B) [80,81], and transitions between higher density of state regions of the MoS_2 band structure (C, D) [80,81].

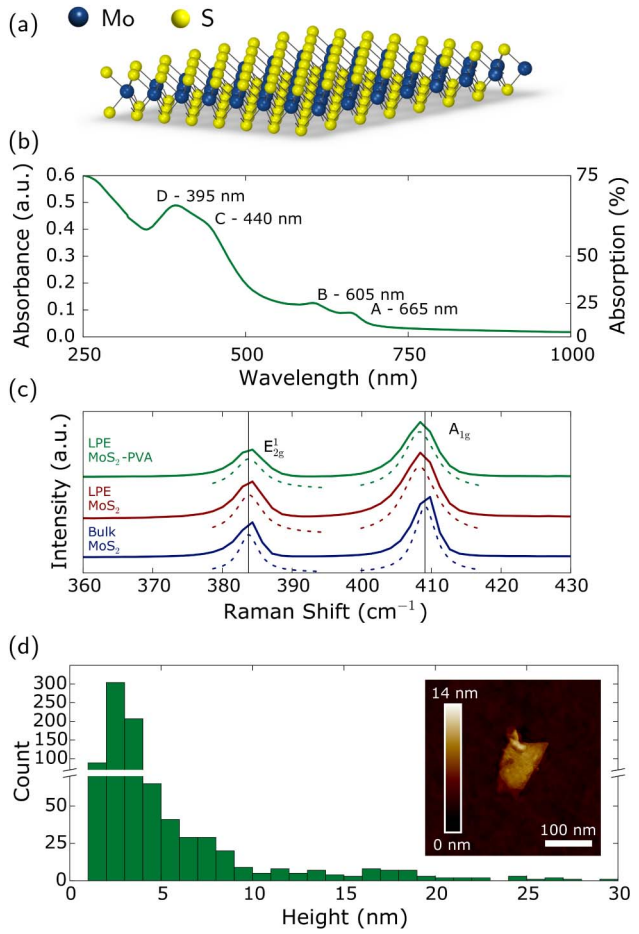

Fig. 1. (a) Illustration of MoS_2 monolayer. (b) Linear optical absorption of MoS_2 dispersion. (c) Raman spectra for the bulk MoS_2, LPE MoS_2, and a MoS_2–polymer composite film. The vertical lines show the peak positions for bulk MoS_2 (obtained by Lorentzian fitting, as shown beneath each peak), highlighting the difference in peak position for LPE and bulk MoS_2. (d) Distribution of flake thicknesses measured via AFM (inset, typical AFM image of MoS_2 flake deposited on Si/SiO_2).

Raman spectroscopy of the sample shows the relative position of the two peaks close to 400 cm^{-1} in the spectrum, corresponding to the E^1_{2g} and A_{1g} vibration modes, and can be used to estimate the number of layers in a sample [57,62,82], since the separation between the peak positions (Δw) increases from 18.7 to 25 cm^{-1} between monolayer and six-layer samples [57], reaching 25.5 cm^{-1} for bulk MoS_2 [57,82]. The spectra for the dispersed MoS_2 flakes and for bulk MoS_2 are shown in Fig. 1(c). For the dispersed MoS_2 flakes, Δw is (24.62 ± 0.02) cm^{-1}, compared with (25.29 ± 0.03) cm^{-1} for bulk MoS_2, confirming the presence of few-layer MoS_2 flakes with estimated 4–6 layer thickness.

Atomic force microscopy (AFM) allows measurement of the distribution of flake thicknesses [Fig. 1(d)], revealing that ~60% of the flakes have thickness 2–4 nm, corresponding to 4–6 layers (assuming ~1 nm measured thickness for a monolayer flake, and ~0.7 nm increase for each subsequent layer [57]), in agreement with the Raman spectroscopy measurements. The average flake dimensions, measured using scanning TEM, are (220 ± 20) nm by (110 ± 10) nm.

The composite SA device is prepared by mixing 4 mL of MoS_2 dispersion with 2 mL of 15 wt. % aqueous PVA solution,

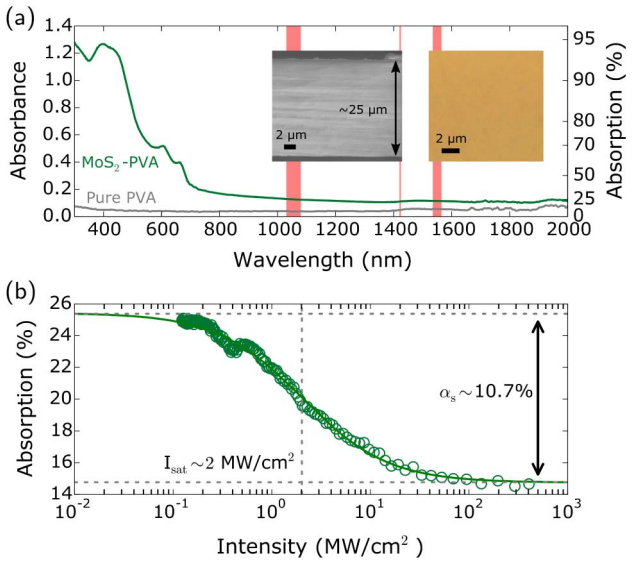

Fig. 2. Optical properties of few-layer MoS_2–PVA composite (after [73]). (a) Linear absorption, compared to pure PVA (red highlighted regions correspond to wavelengths at which MoS_2-based pulsed lasers have been reported); insets show SEM (left) and optical micrograph (right), confirming the absence of large (>1 μm) voids or aggregates; (b) nonlinear absorption of composite film at 1565 nm (0.8 eV).

which is dried in air to form a ~25 μm thick freestanding polymer composite film. The lack of significant shift in the Raman peak positions between the LPE MoS_2 and LPE MoS_2–PVA [Fig. 1(c)] confirms that the MoS_2 structure is unaffected by its inclusion in the composite. Optical microscopy and scanning electron microscopy (SEM) [Fig. 2(a), inset] are used to verify the absence of large (>1 μm) aggregates in the film which could otherwise lead to scattering losses [83], and confirm a uniform distribution of the flakes throughout the composite film. The linear absorption spectrum of the composite is measured along with that of a pure PVA film of the same thickness, showing a measurable difference in the absorption spectra [Fig. 2(a)] even at photon energies below the 1.29 eV material bandgap of few-layer MoS_2, as discussed in Section 3.A.

3. PHOTONIC APPLICATIONS

The unique optical and electronic properties of mono- and few-layer MoS_2, and the potential for its large-scale fabrication through solution-processing techniques indicate that it could be a suitable platform for the development of photonic devices. A strong second-order nonlinearity, $|\chi^2| \sim 10^{-7}$ m/V [84] (from single and odd-numbered layers of the crystal due to broken inversion symmetry) and a high third-order electrical susceptibility, $|\chi^3| \sim 10^{-19}$ m^2/V^2 [85] has been measured, as well as an ultrafast (<100 fs) relaxation time [25]. This highlights the potential for MoS_2 in nonlinear and ultrafast optical applications, including second-harmonic [84,86] and third-harmonic [85] generation, and as a wideband ultrafast SA [25]. Additionally, with a direct bandgap of 1.8 eV in monolayer form, the material exhibits a strong visible photo- and electroluminescence [34,87], opening possibilities for applications including photodetectors and light-emitting diodes.

With a focus on short-pulse laser technology, in the forthcoming sections we discuss the nonlinear optical properties of MoS_2 and collate complete tables of SA devices and pulsed

laser demonstrations that utilize MoS_2 to date, before briefly considering the disruptive impact this exciting 2D material has had on other photonic technologies. For a detailed review of the nano- and optoelectronic properties and applications of MoS_2 that are outside the scope of this work, we refer to [21].

A. Nonlinear Optical Properties

SA are devices with a nonlinear optical absorption profile such that their transmission increases (absorption decreases) with increasing incident light intensity [1]. In semiconductor materials, saturable absorption manifests from the excitation of electrons from the valence band to the conduction band under strong illumination by a source of sufficient photon energy, leaving the upper states filled and the material unable to absorb further photons according to the Pauli exclusion principle [1,8]. It should be noted that this mechanism is distinct from graphene that, as a zero-gap material, it exhibits a linear dispersion of electrons around the Dirac point, generating an electron-hole pair for all incident photons, resulting in saturation due to rapid thermalization of electron states and Pauli blocking [16].

Nonlinear optical absorption of materials can be measured using two common techniques: open-aperture Z-scan [88] and I-scan (often referred to as the balanced twin-detector technique) [89,90]. In a Z-scan setup, the sample is swept through the focal plane of a focused train of short optical pulses and the transmission is recorded as a function of position (often in addition to a reference signal for normalization). The spatial position of the sample is mapped to an intensity, allowing continuous control of the incident intensity for a constant input power. To perform an I-scan measurement, which benefits from the option of a fully fiber-integrated setup, a variable average-power pulsed source is split into a test and reference arm, each terminated at two separate detectors, allowing calibration and characterization of the samples' nonlinear optical response as a function of a variable input power.

A variety of models have been developed to describe the nonlinear saturable absorption behavior of materials [25,91]. The absorption α as a function of incident light intensity I can be expressed simply as

$$\alpha(I) = \alpha_0 + \alpha_{\mathrm{NL}} I, \tag{1}$$

where α_0 and α_{NL} are the linear and nonlinear absorption coefficients, respectively. For practical SA devices, a phenomenological model based on the assumption of a two-level system [91], is widely adopted. By using the model to fit to experimentally measured data from I- and Z-scan setups, device parameters can be extracted and used as a performance comparison metric. This model [91], which assumes an instantaneous material response, has also been extended to account for reverse saturable absorption (RSA) effects (where increased absorption is observed under increased incident intensity), a phenomenon encountered in some nanomaterial-based photonic devices [25,55]. If a SA device in a laser cavity exhibits RSA in addition to SA, the pulse-shaping dynamics can be modified. Depending on the strength and threshold of RSA, it has been reported to suppress Q switching and also to limit the achievable pulse energies [92]. The augmented model takes the form

$$\alpha(I) = \frac{\alpha_{\mathrm{s}}}{1 + \frac{I}{I_{\mathrm{s}}}} + \alpha_{\mathrm{ns}} + \beta I, \tag{2}$$

where α_{s} and α_{ns} are the saturable (i.e., modulation depth) and nonsaturable device loss, respectively; I_{s} is the saturation intensity—the intensity which reduces the device absorption by half of the maximum saturable loss (i.e., considering zero α_{ns} and β), and β is an effective RSA coefficient. The nonlinear absorption profile for our case study few-layer MoS_2 SA (Section 2.D) is shown in Fig. 2(b), obtained by a Z-scan experiment at 1565 nm with 750 fs pulses at 17.8 MHz repetition rate. The SA parameters are determined by fitting the data with Eq. (2): $I_{\mathrm{sat}} = 2.0\ \mathrm{MW\,cm^{-2}}$, $\alpha_{\mathrm{s}} = 10.7\%$, $\alpha_{\mathrm{ns}} = 14.7\%$, and RSA is negligible.

Tables 1(a) and 1(b) summarize nonlinear absorption measurements conducted on few-layer MoS_2 in the literature to date: Table 1(a) describes the properties of few-layer MoS_2 dispersion from solution-processing approaches and Table 1(b) presents the parameters for demonstrated MoS_2-based SA devices. The first nonlinear measurements were performed by Wang *et al.* [25] using a Z-scan setup (with an 800 nm source of 100 fs pulses at 1 kHz repetition frequency) and LPE-fabricated few-layer MoS_2 flakes in N-methylpyrrolidone (NMP), with average flake thickness of 5–6 layers and lateral dimensions <200 nm. Saturable absorption was observed due to carrier excitation through single-photon absorption at 800 nm (1.55 eV). However, it was argued that two-photon absorption (TPA) could also be observed due to a small fraction of monolayer flakes with ~1.8 eV energy gap, greater than the incident photon energy. The saturation intensity was measured as $I_{\mathrm{s}} = 413\ \mathrm{GW\,cm^{-2}}$ and the nonlinear absorption was $-4.6 \times 10^{-3}\ \mathrm{cm\,GW^{-1}}$. The nonlinear absorption coefficient is also occasionally referred to as the TPA coefficient, so a negative α_{NL} refers to SA. Using the same experimental setup and a graphene dispersion, it was concluded that MoS_2 possesses a larger SA response in its resonant band [25]. The MoS_2 intraband relaxation time was also computed as ~30 fs [25] and interband transitions have been reported on picosecond timescales [93]. The two timescales suggest ideal SA behavior: the longer relaxation route aids pulsed-laser self-starting, whereas the ultrafast relaxation enables ultrashort pulse generation, similar to the two timescales exhibited by graphene [16].

Other works have suggested that the average number of layers in MoS_2 flakes can determine whether the nonlinear response is in the SA or RSA regime. Cyclohexylpyrrolidone dispersions containing 15-layer-thick and 6-layer-thick flakes were characterized using Z-scan at 1030 nm (1.20 eV, corresponding to the bulk MoS_2 bandgap) [94]. The dispersion with an average of 15-layer flakes exhibited SA, corresponding to single-photon absorption, but the 6-layer flake dispersion showed TPA, which the authors concluded was due to the increased bandgap energy of few-layer flakes [94]. Strong SA has also been widely observed for excitation with photon energies exceeding the monolayer bandgap, e.g., at 532 nm (2.33 eV) [55,94].

A behavioral dependence on the lateral and longitudinal flake size was also reported for flakes with constant thickness of ~4.9 nm (<7 layers) [55]. By varying the centrifugation speed during the LPE process, it is possible to tune the resulting flake size. Zhou *et al.* [55] found that Z-scans performed on larger flakes (>100 nm lateral/longitudinal lengths) at 532 nm

Table 1. Nonlinear Absorption Parameters for Few-Layer MoS_2 Flakes in Dispersions and Sa Devices

(a) Few-Layer MoS_2 Flakes in Dispersions

Fabrication Method	Dispersed In	MoS_2 Flake Size		Nonlinear Characterization Setup				I_s (GW cm^{-2})	α_0 (cm^{-1})	α_{NL} (cm GW^{-1})	Ref.
		# Layers	Lateral Size (nm)	Z/I	λ	t	f_{rep}				
SP-LPE	NMP	5–6	<200	Z	800 nm	100 fs	1 kHz	413	2.37	-4.60×10^{-3}	[25]
	NVP	5–6	<200	Z	800 nm	100 fs	1 kHz	833	1.66	-1.78×10^{-3}	[25]
	CHP	5–6	<200	Z	800 nm	100 fs	1 kHz	405	2.85	-5.80×10^{-3}	[25]
		~15	–	Z	515 nm	340 fs	1 kHz	58	25.34	–0.357	[94]
		~15	–	Z	532 nm	100 ps	10 kHz	1.13	25.7	–26.2	[94]
		~15	–	Z	800 nm	100 fs	1 kHz	381	11.2	-2.42×10^{-2}	[94]
		~15	–	Z	1030 nm	340 fs	1 kHz	114	11.8	-9.17×10^{-2}	[94]
		~6	–	Z	1030 nm	340 fs	1 kHz	–	0.034	$+8.0 \times 10^{-5}$ (RSA)	[94]
		~15	–	Z	1064 nm	100 ps	10 kHz	2.1	11.6	–5.5	[94]
	Ethanol/H_2O	<7	<500 nm	Z	532 nm	19 ps	10 Hz	~1	–	>7% SA[a]	[55]
		<7	~100 nm	Z	532 nm	19 ps	10 Hz	~1	–	>5% SA[a]	[55]
		<7	~50–60 nm	Z	532 nm	19 ps	10 Hz	~1	–	(RSA)	[55]
SP-I	IPA	1–3	–	Z	400 nm	100 fs	1 kHz	136	–	10% SA[a]	[66]
		1–3	–	Z	800 nm	100 fs	1 kHz	280	–	34% SA[a]	[66]
		1–3	–	I	800 nm	100 fs	1 kHz	338	–	33% SA[a]	[66]

(b) Few-Layer MoS_2 Flakes Integrated to Form SA Devices

Fabrication Method	Integration Platform	MoS_2 Flake Size		Nonlinear Characterization Setup				I_s (MW cm^{-2})	Modulation Depth, α_s (%)	Unsaturable Loss, α_{ns} (%)	Ref.
		# Layers	Lateral Size (nm)	Z/I	λ	t	f_{rep}				
SP-LPE	PVA composite	3–4	–	I	1560 nm	250 fs	22.2 MHz	10	2	48.5	[74]
		4–5	~220	Z	1065 nm	500 fs	26.4 MHz	1.6	6.3	18.0	[72]
		4–5	~220	Z	1565 nm	750 fs	17.8 MHz	2.0	10.7	14.7	[73]
		~3	–	I	1566 nm	212 fs	22.0 MHz	13	1.6	54.8	[75]
	BK7 glass	~3	–	I	1560 nm	250 fs	22.0 MHz	13	–	–	[69]
SP-I	Microfiber	1–3	–	I	1041 nm	~ ps	6.54 MHz	–	10.5	78.0	[49]
		4–5	–	I	1554 nm	500 fs	26.0 MHz	–	2.8	57.3	[48]
	PVA	4–5	–	I	1554 nm	500 fs	26.0 MHz	34	4.3	24	[47]
	Quartz	1–3	–	Z	800 nm	100 fs	1 kHz	1850	15.9	–	[66]
CVD	Fiber facet	4–5	–	I	1550 nm	250 fs	20.0 MHz	0.34	35.4	34.1	[77]
		4–5	–	I	1550 nm	250 fs	20.0 MHz	0.43	33.2	35	[79]
	Side-polished fiber	<10	100–400	I	1563 nm	800 fs	–	>100	>2.5	<70	[78]
ME	Fiber facet	1–8	–	I	1552 nm	–	–	–	>2.1	<90	[76]
PLD	Quartz	~30	–	Z	1060 nm	40 ps	–	2450	27	–	[42]
HTG	PVA composite	3–10	–	I	1030 nm	–	–	18	10.7	39	[41]

Note: Where distributions of MoS_2 flake sizes were reported, we quote the average flake dimensions. SP-I, solution processed using intercalation; SP-LPE, solution processed using LPE; ME, mechanical exfoliation; HTG, hydrothermal growth; NMP; NVP, N-vinylpyrrolidone; CHP, cyclohexylpyrrolidone; IPA, isopropyl alcohol. Nonlinear characterization setup parameters: Z/I, Z-/I-scan; λ, wavelength; t, pulse duration; f_{rep}, pulse repetition rate.

exhibited SA behavior, as expected for above-bandgap excitation, but dispersions containing smaller flakes (with 50–60 nm average dimensions) exhibited RSA. Using transient absorption spectroscopy, they showed that excited state absorption (ESA) was the responsible mechanism, proposing that the difference in behavior for large and small flakes was due to an increased proportion of edge defects in smaller flakes. It was proposed that unsaturated edges could create localized edge states within the bandgap, assisting the excitation of electrons into the conduction band. However, edge states can be quenched at higher powers, leading to RSA behavior [55]. In graphene, due to the zero bandgap, edge states are not involved in the absorption mechanism [55].

A transition from SA to RSA behavior with increasing incident intensity has also been reported by Ouyang *et al.* [95], at 532 nm for 100–200 nm sized flakes with <10 nm thickness (<14 layers) deposited on quartz (importantly, the process was reversible, indicating that the sample was not suffering photo damage at higher energies). Their analysis showed that ESA played a dominant role in the process [95]. Zhang *et al.* [66] made similar observations of a power-dependent transition from SA to RSA behavior for intercalated 1–3 layer MoS_2 flakes in an IPA dispersion, which was attributed to nonlinear scattering from the formation of microbubbles around the nanomaterial in the host dispersion at high intensities [66].

In addition to studies of the fundamental material properties, manufactured SA devices, based on a variety of integration schemes, have also been characterized and used in short-pulse lasers. To date, all MoS_2-based pulsed lasers have operated at wavelengths longer than 1030 nm, perhaps linked to greater availability of gain media (especially in fiber) for such wavelength regions. We note that this corresponds to photon energies lower than the material bandgap for monolayer, few-layer, and even bulk MoS_2. For a perfect crystal, absorption of a single photon with an energy lower than transitions at the fundamental energy gap (leading to the excitation of carriers) is forbidden [96,97].

While multiphoton absorption (including TPA) can occur, this would yield optical limiting behavior rather than SA

[96,97], and hence a question persists: how can few-layer MoS_2 devices behave as SAs at photon energies lower than the material bandgap? In fact, few-layer MoS_2 is not an infinite, perfect crystal; boundary effects, edges, and defects will contribute to a modification of the absorption spectrum [42,55,96,98–101]. Wang *et al.* [42] proposed an explanation based on atomic defects, following theoretical studies of the bandgap behavior using the planewave basis Vienna *ab initio* simulation package (VASP). The introduction of both Mo and S defects can reduce the bandgap, although an excess of Mo defects leads to metallic behavior with no SA effects, whereas S defects maintain the semiconductor behavior and can reduce the bandgap to 0.08 eV (supporting the generation of photoexcited carriers up to wavelengths as long as 15.4 μm, and consequently SA by Pauli blocking).

Recently, we proposed a complementary explanation based on edge-state absorption [72], supported by early studies on few-layer MoS_2. Specifically, Roxlo *et al.* [98–100] performed photothermal deflection spectroscopy (PDS) measurements to characterize the absorption (noting PDS is unaffected by scattering) of different sizes of few-layer MoS_2 flakes at photon energies above and below the bandgap. They found very similar absorption spectra for photoexcitation at wavelengths corresponding to energies higher than the material bandgap, but at sub-bandgap wavelength-equivalent energies, small flakes of few-layer MoS_2 (~1 μm across) showed up to two orders of magnitude greater absorption than a single crystal. Texturing of single crystals has also been shown to increase sub-bandgap absorption by a factor of 10 [99,100]. Smaller or textured flakes possess a larger edge to surface area ratio, suggesting a greater contribution to the absorption spectra from edge states that form quasi-energy levels within the forbidden energy gap of the pristine crystal band structure [96,98–100]. The appearance of edge sites in the bandgap could explain observations of absorption at photon energies lower than the single MoS_2 crystal bandgap that, when saturated at high intensities by Pauli blocking, lead to SA behavior [72]. This mechanism for SA is supported by reports of mode-locking using defect in-bandgap states in other nonlinear crystals [102,103], in addition to recent reports of enhanced nonlinear optical processes at few-layer MoS_2 flake edges [101].

The nonlinear sub-bandgap absorption of few-layer MoS_2 SA devices, designed specifically for use in laser cavities, has been measured at ~1060 [41,42,49,72] and ~1550 nm [47,73–79]. A wide range of parameters have been reported (see Table 1) with saturation intensities from $<1\ MW\,cm^{-2}$ [77,79] to $2.45\ GW\,cm^{-2}$ [42]; modulation depths between 1.6% [75] and 35.4% [77]; and nonsaturable loss values from 14.7% [73] to ~90% [76]. Wide variation is even observed between devices produced using the same few-layer MoS_2 flake fabrication methods and integration platforms. Since the ideal SA parameters depend on the type of laser being designed and whether mode-locked or *Q*-switched operation is desired [1], the range of parameters offered by MoS_2 SAs and ability to engineer their performance is beneficial. Devices containing a variety of average MoS_2 flake thicknesses, from ~3 [49,66,69,74,75] to ~30 [42] layers have been demonstrated as SAs at numerous wavelengths which correspond to sub-bandgap absorption (incident photon energy less than the bandgap). Such wideband SA behavior could be attributed to a distribution of edge states within the bandgap [72]. However, the nonsaturable loss of devices to date is high (often >20%), which could limit the application of such devices in lower gain systems, including diode-pumped solid-state lasers [104].

B. MoS_2-Based Short-Pulse Lasers

Short-pulse lasers can loosely be categorized as coherent light sources generating pulses on the order of several microseconds, nanoseconds, or even few femtoseconds in duration (where the latter group is typically termed ultrafast lasers). The pulsed mode of a laser can be initiated by the inclusion of a SA to act as a passive optical switch. Depending on the parameters of the SA such as its strength of absorption (or modulation depth) or characteristic recovery time, and the design of the laser cavity, distinct regimes of operation exist that have qualitatively and quantitatively different characteristics [1,2].

In *Q*-switched lasers, the SA modulates the laser cavity *Q* factor: when the absorber is unsaturated, the *Q* factor is low and thus energy in the gain medium accumulates; as the intracavity energy increases, the absorber saturates, rapidly increasing the *Q* factor and the laser pulse power, allowing efficient extraction of energy stored in the gain medium in a single giant pulse. After the *Q* switch, the absorber and the gain recover. *Q*-switched laser pulses are typically characterized by [1,2]:

- high-energy (μJ–mJ);
- low repetition frequency (kHz);
- μs–ns duration.

Consequently, *Q*-switched lasers target applications such as materials processing, where energetic pulses are required to remove or ablate material [4]. In a distinct regime, known as mode-locking, the SA applies a modulation with a periodicity equal to the cavity roundtrip time, coupling longitudinal cavity modes and locking their phases, generating a train of pulses. Mode-locked laser pulses are typically characterized by [1,2]:

- lower energy compared to *Q*-switched lasers (pJ–μJ);
- higher repetition rate (MHz–GHz); and
- shorter duration (ps–fs).

Mode-locked lasers are suitable for high peak power, low average power, time-resolved applications such as optical metrology and biophotonic imaging [3]. In both regimes, the properties of the SA play a central role in defining laser operation; thus new materials for SA devices that exhibit wideband intensity-dependent absorption with a high modulation depth, ultrafast response, and low nonsaturable loss, in addition to environmental robustness, are in great demand.

Since the successful exfoliation and characterization of the optical properties of 2D MoS_2, there have been a number of demonstrations of short-pulse laser operation utilizing the semiconducting nanomaterial; similar to graphene, heralded for its potential for broadband, ultrafast switching operation. Table 2 summarizes the parameters and properties of lasers based on MoS_2 SAs to date. The majority of pulsed lasers using MoS_2 have employed fiber gain media [47–49,66,71–79], although MoS_2 SAs have also been successfully deployed in bulk lasers [41,42,69]. However, it should be noted that the numerous advantages of fiber lasers such as high gain; their alignment-free, monolithic architecture; and efficient heat dissipation relax the requirements of the SA. Fiber systems can

typically tolerate higher nonsaturable losses that are prohibitive in bulk lasers [67].

The first short-pulse laser using a few-layer MoS_2 SA was a bulk *Q*-switched cavity, reported by Wang *et al.* [42], followed by the first demonstration of a MoS_2-based *Q*-switched fiber laser by Woodward *et al.* [71]. Since then, numerous other few-layer MoS_2-based *Q*-switched lasers have been reported, operating over a wide wavelength range, including operation at: ~1060 [41,42,69,71,72,75], 1420 [42], ~1550 [74–76,79], 2032 [75], and 2100 nm [42] (Table 2). Demonstrations also include tunable operation over the Yb gain band (1030–1070 nm) [72] and Er gain band (1520–1568 nm) [74], further confirming the wideband operation of few-layer MoS_2 SAs. A typical design for a *Q*-switched fiber laser is shown in Fig. 3(a) (after [72]), in addition to the measured output properties [Figs. 3(b)–3(d)] showing a 74 kHz pulse train, 2.88 μs duration pulse, and representative laser spectra from within the tunable operating range. Bulk *Q*-switched lasers have generated pulses at much greater output powers (>200 mW) than their fiber counterparts (typically <10 mW), which suggests a high damage threshold of SAs employing few-layer MoS_2 on glass substrates, although the exact intensity on the device was unreported. The highest average output power of 260 mW [69], corresponding to a pulse energy of 1.1 μJ, suggests such sources could be applied in medical therapeutics or for material processing [4].

The first mode-locked laser using a MoS_2 SA was reported by Zhang *et al.*, based on a Yb:fiber laser [66]. Subsequently, numerous other MoS_2 mode-locked fiber lasers have been reported within both Yb and Er gain bands, with a wide range of output powers, pulse durations, and repetition rates. All MoS_2 mode-locked lasers to date have employed unidirectional ring cavity designs; the highest reported output power is 9.3 mW, corresponding to a maximum pulse energy of 1.4 nJ. The highest peak power generated to date is ~420 W [77], and the highest repetition frequency—mode locking at the 369th cavity harmonic—is 2.5 GHz [48]. Pulse generation in both the net-anomalous soliton and all-normal dispersion regimes have been observed, with the shortest pulse duration recorded as 710 fs [47]. A continuously tunable mode-locked laser from 1535–1565 nm, producing picosecond pulses (Fig. 4), has also been reported, highlighting the broadband operation of MoS_2-based SAs [73]. A bulk mode-locked laser employing few-layer MoS_2 has yet to be demonstrated, possibly due to the high nonsaturable loss of current MoS_2 SAs, which could preferentially support *Q*-switched operation over mode locking [1,2], although with further improvements to fabrication and integration procedures to produce low-loss SA devices, we expect that this will soon be possible.

C. Other Devices

The scope of this work has been restricted to a discussion of mono- and few-layer MoS_2-based devices from the perspective of short-pulse laser technology, using the devices as SAs to promote pulsed operation either by the mechanisms of *Q* switching or mode locking. In this section, we briefly consider other photonic applications of 2D MoS_2.

Distinct from the semimetallic nature of graphene, the direct gap semiconducting properties of monolayer MoS_2, which efficiently absorbs and emits photons via transitions at the fundamental energy gap [23], supports opportunities for the optoelectronic and photonic application of 2D materials

Table 2. Pulsed Lasers with Few-Layer MoS_2 SAs

Laser Type	Few-Layer MoS_2 Fabrication Method	Integration Platform	# Layers in MoS_2 Flakes	λ (nm)	Laser Properties			Ref.
					t	f_{rep}	P (mW)	
Mode-Locked								
Yb:Fiber	SP-I	Microfiber	1–3	1043	656 ps	6.7 MHz	2.4	[49]
		Fiber facet	1–3	1054	800 ps	6.6 MHz	9.3	[66]
Er:Fiber	CVD	Fiber facet	4–5	1569	1.28 ps	8.3 MHz	5.1	[77]
		Side-polished fiber	<10	1568	4.98 ps	26.0 MHz	2.0	[78]
		Side-polished fiber	<10	1568	637 fs	33.5 MHz	–	[78]
	SP-LPE	PVA composite	4–5	1535–1565 tunable	~1 ps	13.0 MHz	–	[73]
	SP-I	PVA composite	4–5	1570	710 fs	12.1 MHz	1.8	[47]
		Microfiber	4–5	1558	3 ps	2.5 GHz	5.4	[48]
Q-Switched								
Yb:Fiber	SP-LPE	PVA composite	4–5	1068	2.7 μs	67 kHz	0.5	[71]
		PVA composite	4–5	1030–1070 tunable	2.7 μs	89 kHz	10.3	[72]
		PVA composite	~3	1067	10.7 μs	13.4 kHz	0.9	[75]
$Nd:GdVO_4$	PLD	Quartz	~30	1060	970 ns	732 kHz	227	[42]
$Nd:YAlO_3$	SP-LPE	BK7 glass	~3	1080	227 ns	233 kHz	260	[69]
Nd:YGG	PLD	Quartz	~30	1420	729 ns	77 kHz	52	[42]
Yb:YAG	HTG	PVA composite	3–10	1030	12 μs	17 kHz	250	[41]
Er:Fiber	SP-LPE	PVA composite	3–4	1520–1568 tunable	5 μs	35 kHz	1.5	[74]
		PVA composite	~3	1565	7.5 μs	11.9 kHz	1.7	[75]
	CVD	Fiber facet	4–5	1550	1.6 μs	173 kHz	4.7	[79]
	ME	Fiber facet	1–8	1563	3.9 μs	41 kHz	3.5	[76]
Tm:Fiber	SP-LPE	PVA composite	~3	2032	2.06 μs	38.4 kHz	47.3	[75]
Tm:Ho:YGG	PLD	Quartz	~30	2100	410 ns	149 kHz	206	[42]

Note: Where ranges of parameters were reported for *Q*-switched lasers due to the power-dependent repetition rate and pulse duration, we quote the properties at the maximum power. SP-I, solution processed using intercalation; SP-LPE, solution processed using LPE; ME, mechanical exfoliation; HTG, hydrothermal growth; λ, operating wavelength; t, pulse duration; f_{rep}, pulse repetition rate; P, average output power.

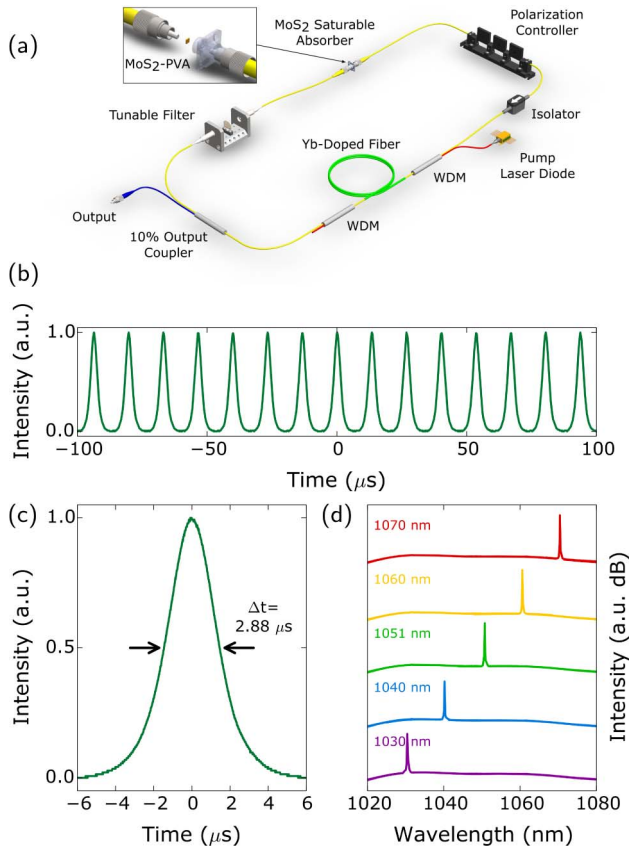

Fig. 3. Tunable MoS_2 *Q*-switched fiber laser (after [72]): (a) cavity schematic, (b) output 74 kHz pulse train, (c) profile of single pulse, (d) various spectra at wavelengths within the continuous tuning range of 1030–1070 nm.

not previously exploited, including nanoscale electro-optic modulators at visible frequencies [105], photodetectors with high responsivity [61,106,107], light-emitting diodes [87], and solar cells [108,109]. Similarly, a lack of inversion symmetry in single and odd layers of MoS_2 differentiates prospective applications compared to those of graphene, not least giving rise to a finite second-order optical nonlinearity ($\chi^2 \neq 0$), leading to observations of intense second-harmonic generation from

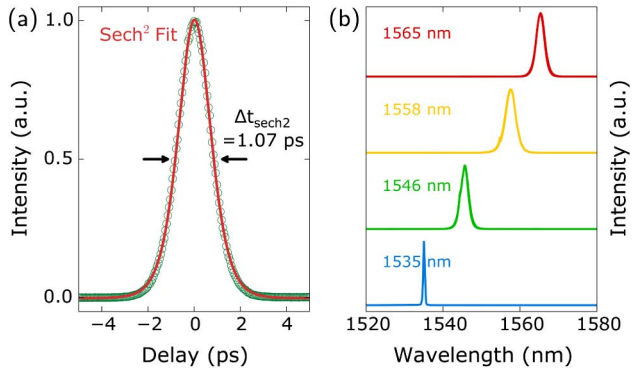

Fig. 4. Tunable MoS_2 mode-locked fiber laser characteristics (after [73]): (a) typical autocorrelation trace, (b) various spectra at wavelengths within the continuous tuning range of 1535–1565 nm. Spectral narrowing towards shorter wavelengths is due to overlapping with the fall-off of the amplifier gain bandwidth (and resulted in longer pules [73]).

monolayer crystals of the material [84,101,110], and the ability to optically control the valley polarization state [111,112], allowing new opportunities in the emergent field of *valleytronics* [113]. Due to a large elastic strain that monolayers of the material can accommodate, bandgap engineering of MoS_2 permits tailoring of its optical properties [114].

The favorable optical properties of MoS_2 can be further enhanced by vertical hybrid heterostructuring, where single layers form trap-free binary or multilayered devices with graphene (known as G-TMD stacks) [115,116], or indeed another layered 2D semiconductor from the TMD family of materials (TMD–TMD stacks) [117–119]. Both material systems are receiving considerable attention, from a theoretical and experimental perspective, because of the highly engineerable architecture due to the dangling-bond-free surfaces of 2D crystals and the ability to readily form semiconductor junctions with the desired band alignment due to the library of available 2D materials. In the case of TMD–TMD stacks, similar crystal structure and growth conditions support synthesis and large-scale fabrication using CVD, while providing another route to modification of the electronic band structure. Among a number of advantages, G-TMDs exploit the high mobility in graphene, leading to fast response times, and the strong visible absorption of MoS_2 to form devices such as photodetectors exhibiting an ultra-high photo gain [116].

Despite the fact that TMDs such as MoS_2 are heralded as exhibiting strong light absorption at energies corresponding to their exciton resonances, due to their atomically thin nature and consequently short absorption lengths, 2D materials possess weak light–matter interactions in absolute terms [117]. Multilayers offering stronger absorption mitigate this paradox; however, the benefits of a 2D structure, including strong quantum confinement, can be compromised. This inherently weak optical interaction can potentially be circumvented, or the interaction enhanced, through a unison with plasmonic nanostructures where the excitation of plasmonic surface modes can achieve a strong change in the optical response of a nearby material layer [117].

4. CONCLUSION AND OUTLOOK

The recent research interest in few-layer MoS_2 has revealed numerous excellent optoelectronic properties exploitable for future photonic applications. For short-pulse laser technology, the nonlinear optical properties are of particular interest: few-layer MoS_2 exhibits a broadband nonlinear response, showing both saturable absorption and RSA (Table 1). The nature and strength of the nonlinear response has been found to depend on the layer count of processed few-layer MoS_2 flakes (i.e., flake thickness) [94], lateral/longitudinal flake dimensions [55], and on the device integration scheme. It is worth noting that many studies to date have considered processing methods producing a distribution of flake dimensions [25,73]. Flakes of different sizes exhibit distinct characteristics [25,55,120]; the dominant device behavior corresponds to the average flake size, suggesting that statistical methods are needed to understand and analyze device performance. This dependence allows the engineering of the optical properties of few-layer MoS_2 devices over a wide range.

The reported wideband behavior of MoS_2 SAs is very promising, enabling one few-layer MoS_2-based SA device to operate at many different laser wavelengths (Table 2). At excitation

photon energies greater than the material bandgap, the SA mechanism has been explained by single-photon absorption exciting electrons into the conduction band, followed by Pauli blocking [25,55,72,95]. For photon energies lower than the bandgap, TPA and ESA have been reported as absorption mechanisms giving rise to RSA behavior [25]. However, sub-bandgap SA behavior has also been reported [55,72]. While single-photon absorption is forbidden in a perfect infinite crystal [96], the finite-sized 2D flakes of few-layer MoS_2 possess a high edge to surface area ratio [55,72]. These defect sites [42] and edge states [72,99] may support absorption of light at wavelengths longer than the wavelength equivalent bandgap energy, and consequently can exhibit SA through Pauli blocking at high intensities [42,72].

With regards to integration, a wide variety of platforms have been reported using few-layer MoS_2 flakes from a range of processing techniques, including embedding flakes in a PVA composite; direct deposition onto fiber facets, microfibers, and side-polished fibers; and also deposition onto quartz/BK7 glass. These SA devices have been used to *Q* switch and mode lock both bulk and fiber lasers from 1030 to 2100 nm, enabling laser pulse generation at kilohertz to gigahertz repetition rates and with few microsecond to sub-picosecond pulse durations. The output powers of MoS_2-based lasers to date have been modest, typically a few milliwatts for fiber lasers, although extracavity amplification and power scaling in master-oscillator power amplifier configurations is expected to lead to higher achievable powers [121]. For fiber lasers, nonlinear effects can limit the maximum achievable peak power [121], although recent progress suggests a route to high-pulse-energy fiber lasers by using large-mode-area fiber [122] and novel all-normal dispersion, long-cavity designs that produce low-repetition-rate trains of high-energy giant-chirped pulses, suitable for compact chirped pulse amplification and compression setups [123,124]. The inclusions of few-layer MoS_2-based SAs in other laser platforms, such as thin-disk and vertical external cavity surface emitting lasers is also expected, offering greater versatility and power scalability [125]. However, the high nonsaturable loss of current MoS_2 SAs could present problems for their application in bulk systems; further work is needed to lower this loss while maintaining the high saturable component.

The performance properties of few-layer MoS_2 SAs, such as ultrafast material relaxation time [25], fabrication and integration flexibility [18], and the potential for wideband operation throughout the near-IR [42,72] are comparable to other nanomaterial-based SAs, including graphene and carbon nanotubes [15,16,67]. However, the potential for application of few-layer MoS_2 SAs at visible wavelengths, around the peak of the fundamental exciton resonance [22], offers a tangible advantage over competing technologies. The required tube diameter to achieve strong visible resonant absorption in nanotubes presents fabrication difficulties [15], and the saturation intensity of graphene is reported to scale inversely with wavelength [17], which is unfavorable for visible lasers. However, monolayer MoS_2 has a direct 1.80 eV bandgap [22] (equivalent to a wavelength of 689 nm) and the bandgap for few-layer crystals can also correspond to energies in the visible spectral range. Indeed, existing MoS_2 studies have experimentally confirmed saturable absorption at 532 nm [55,94], paving the way for visible short-pulse lasers using few-layer MoS_2 SA devices.

Finally, we note that MoS_2 is only one material within the family of TMDs. Numerous studies discussed in this review also considered the nonlinear optical properties of other semiconducting TMDs, such as $MoSe_2$ and WS_2, observing similarly strong SA and RSA responses from these layered materials. The explanations for layer-dependent properties and edge-driven sub-bandgap absorption could apply to other few-layer TMDs, suggesting their application as SAs for short-pulse lasers. Indeed, few-layer tungsten disulfide (WS_2) SAs are beginning to emerge [126–129]. However, further work is still required to critically evaluate their properties. Additionally, vertical hybrid heterostructuring of TMDs represents a new material system, with promising optical properties that could allow even greater control and engineering of laser pulse sources.

ACKNOWLEDGMENTS

The authors would like to thank J. R. Taylor for fruitful discussions. E. J. R. K. and T. H. acknowledge support from the Royal Academy of Engineering (RAEng).

REFERENCES

1. O. Svelto, *Principles of Lasers* (Springer, 2010).
2. A. E. Siegman, *Lasers* (University Science Books, 1990).
3. F. Dausinger, F. Lichtner, and H. Lubatschowski, *Femtosecond Technology for Technical and Medical Applications* (Springer, 2004).
4. W. M. Steen and J. Mazumder, *Laser Material Processing* (Springer, 2010).
5. B. H. Chapman, E. J. R. Kelleher, K. M. Golant, S. V. Popov, and J. R. Taylor, "Amplification of picosecond pulses and gigahertz signals in bismuth-doped fiber amplifiers," Opt. Lett. **36**, 1446–1448 (2011).
6. N. D. Psaila, R. R. Thomson, H. T. Bookey, A. K. Kar, N. Chiodo, R. Osellame, G. Cerullo, A. Jha, and S. Shen, "Er:Yb-doped oxyfluoride silicate glass waveguide amplifier fabricated using femtosecond laser inscription," Appl. Phys. Lett. **90**, 131102 (2007).
7. U. Keller, K. J. Weingarten, F. X. Kartner, D. Kopf, B. Braun, I. D. Jung, R. Fluck, C. Honninger, N. Matuschek, and J. Aus der Au, "Semiconductor saturable absorber mirrors (SESAMs) for femtosecond to nanosecond pulse generation in solid-state lasers," IEEE J. Quant. Electron. **2**, 435–453 (1996).
8. U. Keller, "Recent developments in compact ultrafast lasers," Nature **424**, 831–838 (2003).
9. K. Tamura, H. A. Haus, and E. P. Ippen, "Self-starting additive pulse mode-locked erbium fibre ring laser," Electron. Lett. **28**, 2226–2228 (1992).
10. S. Iijima, "Helical microtubules of graphitic carbon," Nature **354**, 56–58 (1991).
11. P. Avouris, M. Freitag, and V. Perebeinos, "Carbon-nanotube photonics and optoelectronics," Nat. Photonics **2**, 341–350 (2008).
12. K. Novoselov, A. Geim, S. Morozov, D. Jiang, Y. Zhang, S. V. Dubonos, I. V. Grigorieva, and A. A. Firsov, "Electric field effect in atomically thin carbon films," Science **306**, 666–669 (2004).
13. F. Bonaccorso, Z. Sun, T. Hasan, and A. C. Ferrari, "Graphene photonics and optoelectronics," Nat. Photonics **4**, 611–622 (2010).
14. S. Set, H. Yaguchi, Y. Tanaka, and M. Jablonski, "Ultrafast fiber pulsed lasers incorporating carbon nanotubes," IEEE J. Sel. Top. Quantum Electron. **10**, 137–146 (2004).
15. T. Hasan, Z. Sun, F. Wang, F. Bonaccorso, P. H. Tan, A. G. Rozhin, and A. C. Ferrari, "Nanotube-polymer composites for ultrafast photonics," Adv. Mater. **21**, 3874–3899 (2009).
16. Z. Sun, T. Hasan, F. Torrisi, D. Popa, G. Privitera, F. Wang, F. Bonaccorso, D. M. Basko, and A. C. Ferrari, "Graphene mode-locked ultrafast laser," ACS Nano **4**, 803–810 (2010).

17. Q. Bao, H. Zhang, Y. Wang, Z. Ni, Y. Yan, Z. X. Shen, K. P. Loh, and D. Y. Tang, "Atomic-layer graphene as a saturable absorber for ultrafast pulsed lasers," Adv. Funct. Mater. **19**, 3077–3083 (2009).
18. Q. H. Wang, K. Kalantar-Zadeh, A. Kis, J. N. Coleman, and M. S. Strano, "Electronics and optoelectronics of two-dimensional transition metal dichalcogenides," Nat. Nanotechnol. **7**, 699–712 (2012).
19. M. Z. Hasan and C. L. Kane, "Colloquium: Topological insulators," Rev. Mod. Phys. **82**, 3045–3067 (2010).
20. J. A. Wilson and A. Yoffe, "The transition metal dichalcogenides discussion and interpretation of the observed optical, electrical and structural properties," Adv. Phys. **18**, 193–335 (1969).
21. R. Ganatra and Q. Zhang, "Few-layer MoS_2: a promising layered semiconductor," ACS Nano **8**, 4074–4099 (2014).
22. R. G. Dickson and L. Pauling, "The crystal structure of molybdenite," J. Am. Chem. Soc. **45**, 1466–1471 (1923).
23. A. Splendiani, L. Sun, Y. Zhang, T. Li, J. Kim, C.-Y. Chim, G. Galli, and F. Wang, "Emerging photoluminescence in monolayer MoS_2," Nano Lett. **10**, 1271–1275 (2010).
24. B. Radisavljevic, A. Radenovic, J. Brivio, V. Giacometti, and A. Kis, "Single-layer MoS_2 transistors," Nat. Nanotechnol. **6**, 147–150 (2011).
25. K. Wang, J. Wang, J. Fan, M. Lotya, A. O'Neill, D. Fox, Y. Feng, X. Zhang, B. Jiang, Q. Zhao, H. Zhang, J. N. Coleman, L. Zhang, and W. J. Blau, "Ultrafast saturable absorption of two-dimensional MoS_2 nanosheets," ACS Nano **7**, 9260–9267 (2013).
26. A. K. Geim and K. S. Novoselov, "The rise of graphene," Nat. Mater. **6**, 183–191 (2007).
27. R. Frindt and A. Yoffe, "Physical properties of layer structures: optical properties and photoconductivity of thin crystals of molybdenum disulphide," Proc. R. Soc. A **273**, 69–83 (1963).
28. R. F. Frindt, "Optical absorption of a few unit-cell layers of MoS_2," Phys. Rev. **140**, A536–A539 (1965).
29. R. F. Frindt, "Single crystals of MoS_2 several molecular layers thick," J. Appl. Phys. **37**, 1928–1929 (1966).
30. P. Joensen, R. F. Frindt, and S. R. Morrison, "Single-layer MoS_2," Mater. Res. Bull. **21**, 457–461 (1986).
31. F. Bonaccorso and Z. Sun, "Solution processing of graphene, topological insulators and other 2D crystals for ultrafast photonics," Opt. Mater. Express **4**, 63–78 (2014).
32. F. Bonaccorso, A. Lombardo, T. Hasan, Z. Sun, L. Colombo, and A. C. Ferrari, "Production and processing of graphene and 2D crystals," Mater. Today **15**, 564–589 (2012).
33. K. S. Novoselov, D. Jiang, F. Schedin, T. J. Booth, V. V. Khotkevich, S. V. Morozov, and A. K. Geim, "Two-dimensional atomic crystals," Proc. Natl. Acad. Sci. U.S.A. **102**, 10451–10453 (2005).
34. K. F. Mak, C. Lee, J. Hone, J. Shan, and T. F. Heinz, "Atomically thin MoS_2: a new direct-gap semiconductor," Phys. Rev. Lett. **105**, 136805 (2010).
35. S. Helveg, J. V. Lauritsen, E. Lægsgaard, I. Stensgaard, J. K. Nørskov, B. S. Clausen, H. Topsøe, and F. Besenbacher, "Atomic-scale structure of single-layer MoS_2 nanoclusters," Phys. Rev. Lett. **84**, 951–954 (2000).
36. Y. Zhan, Z. Liu, S. Najmaei, P. M. Ajayan, and J. Lou, "Large-area vapor-phase growth and characterization of MoS_2 atomic layers on a SiO_2 substrate," Small **8**, 966–971 (2012).
37. Y.-H. Lee, X.-Q. Zhang, W. Zhang, M.-T. Chang, C.-T. Lin, K.-D. Chang, Y.-C. Yu, J. T.-W. Wang, C.-S. Chang, L.-J. Li, and T.-W. Lin, "Synthesis of large-area MoS_2 atomic layers with chemical vapor deposition," Adv. Mater. **24**, 2320–2325 (2012).
38. K.-K. Liu, W. Zhang, Y.-H. Lee, Y.-C. Lin, M.-T. Chang, C.-Y. Su, C.-S. Chang, H. Li, Y. Shi, H. Zhang, C.-S. Lai, and L.-J. Li, "Growth of large-area and highly crystalline MoS_2 thin layers on insulating substrates," Nano Lett. **12**, 1538–1544 (2012).
39. Y.-H. Lee, L. Yu, H. Wang, W. Fang, X. Ling, Y. Shi, C.-T. Lin, J.-K. Huang, M.-T. Chang, C.-S. Chang, M. Dresselhaus, T. Palacios, L.-J. Li, and J. Kong, "Synthesis and transfer of single-layer transition metal disulfides on diverse surfaces," Nano Lett. **13**, 1852–1857 (2013).
40. S. Najmaei, Z. Liu, W. Zhou, X. Zou, G. Shi, S. Lei, B. I. Yakobson, J.-C. Idrobo, P. M. Ajayan, and J. Lou, "Vapour phase growth and grain boundary structure of molybdenum disulphide atomic layers," Nat. Mater. **12**, 754–759 (2013).
41. Y. Zhan, L. Wang, J. Y. Wang, H. W. Li, and Z. H. Yu, "Yb : YAG thin disk laser passively Q-switched by a hydro-thermal grown molybdenum disulfide saturable absorber," Laser Phys. **25**, 025901 (2015).
42. S. Wang, H. Yu, H. Zhang, A. Wang, M. Zhao, Y. Chen, L. Mei, and J. Wang, "Broadband few-layer MoS_2 saturable absorbers," Adv. Mater. **26**, 3538–3544 (2014).
43. V. Fominski, V. Nevolin, R. Romanov, and I. Smurov, "Ion-assisted deposition of MoSx films from laser-generated plume under pulsed electric field," J. Appl. Phys. **89**, 1449 (2001).
44. G. Eda, H. Yamaguchi, D. Voiry, T. Fujita, M. Chen, and M. Chhowalla, "Photoluminescence from chemically exfoliated MoS_2," Nano Lett. **11**, 5111–5116 (2011).
45. J. Zheng, H. Zhang, S. Dong, Y. Liu, C. T. Nai, H. S. Shin, H. Y. Jeong, B. Liu, and K. P. Loh, "High yield exfoliation of two-dimensional chalcogenides using sodium naphthalenide," Nat. Commun. **5**, 2995 (2014).
46. J. N. Coleman, M. Lotya, A. O'Neill, S. D. Bergin, P. J. King, U. Khan, K. Young, A. Gaucher, S. De, R. J. Smith, I. V. Shvets, S. K. Arora, G. Stanton, H.-Y. Kim, K. Lee, G. T. Kim, G. S. Duesberg, T. Hallam, J. J. Boland, J. J. Wang, J. F. Donegan, J. C. Grunlan, G. Moriarty, A. Shmeliov, R. J. Nicholls, J. M. Perkins, E. M. Grieveson, K. Theuwissen, D. W. McComb, P. D. Nellist, and V. Nicolosi, "Two-dimensional nanosheets produced by liquid exfoliation of layered materials," Science **331**, 568–571 (2011).
47. H. Liu, A.-P. Luo, F.-Z. Wang, R. Tang, M. Liu, Z.-C. Luo, W.-C. Xu, C.-J. Zhao, and H. Zhang, "Femtosecond pulse erbium-doped fiber laser by a few-layer MoS_2 saturable absorber," Opt. Lett. **39**, 4591–4594 (2014).
48. M. Liu, X.-W. Zheng, Y.-L. Qi, H. Liu, A.-P. Luo, Z.-C. Luo, W.-C. Xu, C.-J. Zhao, and H. Zhang, "Microfiber-based few-layer MoS_2 saturable absorber for 25 GHz passively harmonic mode-locked fiber laser," Opt. Express **22**, 22841–22846 (2014).
49. J. Du, Q. Wang, G. Jiang, C. Xu, C. Zhao, Y. Xiang, Y. Chen, S. Wen, and H. Zhang, "Ytterbium-doped fiber laser passively mode locked by few-layer molybdenum disulfide (MoS_2) saturable absorber functioned with evanescent field interaction," Sci. Rep. **4**, 6346 (2014).
50. R. Gordon, D. Yang, E. Crozier, D. Jiang, and R. Frindt, "Structures of exfoliated single layers of WS_2, MoS_2, and $MoSe_2$ in aqueous suspension," Phys. Rev. B **65**, 125407 (2002).
51. M. A. Py and R. R. Haering, "Structural destabilization induced by lithium intercalation in MoS_2 and related compounds," Can. J. Phys. **61**, 76–84 (1983).
52. L. Mattheiss, "Band structures of transition-metal-dichalcogenide layer compounds," Phys. Rev. B **8**, 3719–3740 (1973).
53. J. N. Israelachvili, *Intermolecular and Surface Forces* (Academic, 2011).
54. T. J. Mason, *Sonochemistry* (Oxford, 1999).
55. K.-G. Zhou, M. Zhao, M.-J. Chang, Q. Wang, X.-Z. Wu, Y. Song, and H.-L. Zhang, "Size-dependent nonlinear optical properties of atomically thin transition metal dichalcogenide nanosheets," Small **11**, 634 (2015).
56. Y. Feldman, E. Wasserman, D. Srolovitz, and R. Tenne, "High-rate, gas-phase growth of MoS_2 nested inorganic fullerenes and nanotubes," Science **267**, 222–225 (1995).
57. C. Lee, H. Yan, L. E. Brus, T. F. Heinz, J. Hone, and S. Ryu, "Anomalous lattice vibrations of single- and few-layer MoS_2," ACS Nano **4**, 2695–2700 (2010).
58. Y. Zhao, X. Luo, H. Li, J. Zhang, P. T. Araujo, C. K. Gan, J. Wu, H. Zhang, S. Y. Quek, M. S. Dresselhaus, and Q. Xiong, "Interlayer breathing and shear modes in few-trilayer MoS_2 and WSe_2," Nano Lett. **13**, 1007–1015 (2013).
59. A. Molina-Sánchez and L. Wirtz, "Phonons in single-layer and few-layer MoS_2 and WS_2," Phys. Rev. B **84**, 155413 (2011).
60. B. Chakraborty, H. S. S. R. Matte, A. K. Sood, and C. N. R. Rao, "Layer-dependent resonant Raman scattering of a few layer MoS_2," J. Raman Spectrosc. **44**, 92–96 (2013).
61. W. Zhang, J.-K. Huang, C.-H. Chen, Y.-H. Chang, Y.-J. Cheng, and L.-J. Li, "High-gain phototransistors based on a CVD MoS_2 monolayer," Adv. Mater. **25**, 3456–3461 (2013).
62. X. Zhang, W. Han, J. Wu, S. Milana, Y. Lu, Q. Li, A. Ferrari, and P. Tan, "Raman spectroscopy of shear and layer breathing modes in multilayer MoS_2," Phys. Rev. B **87**, 115413 (2013).

63. V. Nicolosi, M. Chhowalla, M. G. Kanatzidis, M. S. Strano, and J. N. Coleman, "Liquid exfoliation of layered materials," Science **340**, 1226419 (2013).
64. F. Torrisi, T. Hasan, W. Wu, Z. Sun, A. Lombardo, T. S. Kulmala, G.-W. Hsieh, S. Jung, F. Bonaccorso, P. J. Paul, D. Chu, and A. C. Ferrari, "Inkjet-printed graphene electronics," ACS Nano **6**, 2992–3006 (2012).
65. F. Withers, H. Yang, L. Britnell, A. P. Rooney, E. Lewis, A. Felten, C. R. Woods, V. S. Romaguera, T. Georgiou, A. Eckmann, Y. J. Kim, S. G. Yeates, S. J. Haigh, A. K. Geim, K. S. Novoselov, and C. Casiraghi, "Heterostructures produced from nanosheet-based inks," Nano Lett. **14**, 3987–3992 (2014).
66. H. Zhang, S. B. Lu, J. Zheng, J. Du, S. C. Wen, D. Y. Tang, and K. P. Loh, "Molybdenum disulfide (MoS_2) as a broadband saturable absorber for ultra-fast photonics," Opt. Express **22**, 7249–7260 (2014).
67. Z. Sun, T. Hasan, and A. C. Ferrari, "Ultrafast lasers mode-locked by nanotubes and graphene," Physica E **44**, 1082–1091 (2012).
68. B. V. Cunning, C. L. Brown, and D. Kielpinski, "Low-loss flake-graphene saturable absorber mirror for laser mode-locking at sub-200-fs pulse duration," Appl. Phys. Lett. **99**, 261109 (2011).
69. B. Xu, Y. Cheng, Y. Wang, Y. Huang, J. Peng, Z. Luo, H. Xu, Z. Cai, J. Weng, and R. Moncorgé, "Passively Q-switched Nd:$YAlO_3$ nanosecond laser using MoS_2 as saturable absorber," Opt. Express **22**, 28934–28940 (2014).
70. R. J. Smith, P. J. King, M. Lotya, C. Wirtz, U. Khan, S. De, A. O'Neill, G. S. Duesberg, J. C. Grunlan, G. Moriarty, J. Chen, J. Wang, A. I. Minett, V. Nicolosi, and J. N. Coleman, "Large-scale exfoliation of inorganic layered compounds in aqueous surfactant solutions," Adv. Mater. **23**, 3944–3948 (2011).
71. R. I. Woodward, E. J. R. Kelleher, T. H. Runcorn, S. V. Popov, F. Torrisi, R. C. T. Howe, and T. Hasan, "*Q*-switched fiber laser with MoS_2 saturable absorber," in *CLEO: 2014*, OSA Technical Digest (Optical Society of America, 2014), paper SM3H-6.
72. R. I. Woodward, E. J. R. Kelleher, R. C. T. Howe, G. Hu, F. Torrisi, T. Hasan, S. V. Popov, and J. R. Taylor, "Tunable *Q*-switched fiber laser based on saturable edge-state absorption in few-layer molybdenum disulfide (MoS_2)," Opt. Express **22**, 31113–31122 (2014).
73. M. Zhang, R. C. T. Howe, R. I. Woodward, E. J. R. Kelleher, F. Torrisi, G. Hu, S. V. Popov, J. R. Taylor, and T. Hasan, "Solution processed MoS_2-PVA composite for sub-bandgap mode-locking of a wideband tunable ultrafast Er:fiber laser," Nano Res., doi:10.1007/s12274-014-0637-2 (to be published)..
74. Y. Huang, Z. Luo, Y. Li, M. Zhong, B. Xu, K. Che, H. Xu, Z. Cai, J. Peng, and J. Weng, "Widely-tunable, passively *Q*-switched erbium-doped fiber laser with few-layer MoS_2 saturable absorber," Opt. Express **22**, 25258–25266 (2014).
75. Z. Luo, Y. Huang, M. Zhong, Y. Li, J. Wu, B. Xu, H. Xu, Z. Cai, J. Peng, and J. Weng, "1-, 1.5-, and 2-um fiber lasers *Q*-switched by a broadband few-layer MoS_2 saturable absorber," J. Lightwave Technol. **32**, 4679–4686 (2014).
76. R. Khazaeinezhad, S. H. Kassani, T. Nazari, H. Jeong, J. Kim, K. Choi, J.-U. Lee, J. H. Kim, H. Cheong, D.-I. Yeom, and K. Oh, "Saturable optical absorption in MoS_2 nano-sheet optically deposited on the optical fiber facet," Opt. Commun. **335**, 224–230 (2015).
77. H. Xia, H. Li, C. Lan, C. Li, X. Zhang, S. Zhang, and Y. Liu, "Ultrafast erbium-doped fiber laser mode-locked by a CVD-grown molybdenum disulfide (MoS_2) saturable absorber," Opt. Express **22**, 17341–17348 (2014).
78. R. Khazaeizhad, S. H. Kassani, H. Jeong, D.-I. Yeom, and K. Oh, "Mode-locking of Er-doped fiber laser using a multilayer MoS_2 thin film as a saturable absorber in both anomalous and normal dispersion regimes," Opt. Express **22**, 23732–23742 (2014).
79. H. Li, H. Xia, C. Lan, C. Li, X. Zhang, J. Li, and Y. Liu, "Passively *Q*-switched erbium-doped fiber laser based on few-layer MoS_2 saturable absorber," IEEE Photon. Technol. Lett. **27**, 69–72 (2015).
80. A. R. Beal, J. C. Knights, and W. Y. Liang, "Transmission spectra of some transition metal dichalcogenides. II. Group VIA: trigonal prismatic coordination," J. Phys. C **5**, 3540–3551 (1972).
81. R. A. Bromley, R. B. Murray, and A. D. Yoffe, "The band structures of some transition metal dichalcogenides: III. Group VIA : trigonal prism materials," J. Phys. C **5**, 759–778 (1972).
82. H. Li, Q. Zhang, C. C. R. Yap, B. K. Tay, T. H. T. Edwin, A. Olivier, and D. Baillargeat, "From bulk to monolayer MoS_2: evolution of Raman scattering," Adv. Funct. Mater. **22**, 1385–1390 (2012).
83. T. Hasan, F. Torrisi, Z. Sun, D. Popa, V. Nicolosi, G. Privitera, F. Bonaccorso, and A. C. Ferrari, "Solution-phase exfoliation of graphite for ultrafast photonics," Phys. Status Solidi B **247**, 2953–2957 (2010).
84. N. Kumar, S. Najmaei, Q. Cui, F. Ceballos, P. Ajayan, J. Lou, and H. Zhao, "Second harmonic microscopy of monolayer MoS_2," Phys. Rev. B **87**, 161403 (2013).
85. R. Wang, H.-C. Chien, J. Kumar, N. Kumar, H.-Y. Chiu, and H. Zhao, "Third-harmonic generation in ultrathin films of MoS_2," ACS Appl. Mater. Interfaces **6**, 314–318 (2014).
86. Y. Li, Y. Rao, K. F. Mak, Y. You, S. Wang, C. R. Dean, and T. F. Heinz, "Probing symmetry properties of few-layer MoS_2 and h-BN by optical second-harmonic generation," Nano Lett. **13**, 3329–3333 (2013).
87. R. Sundaram, M. Engel, A. Lombardo, R. Krupke, A. C. Ferrari, P. Avouris, and M. Steiner, "Electroluminescence in single layer MoS_2," Nano Lett. **13**, 1416–1421 (2013).
88. M. Sheik-Bahae, A. A. Said, T.-H. Wei, D. Hagan, and E. Van Stryland, "Sensitive measurement of optical nonlinearities using a single beam," IEEE J. Quantum Electron. **26**, 760–769 (1990).
89. B. Taheri, H. Liu, B. Jassemnejad, D. Appling, R. C. Powell, and J. J. Song, "Intensity scan and two photon absorption and nonlinear refraction of C60 in toluene," Appl. Phys. Lett. **68**, 1317 (1996).
90. R. F. Souza, M. A. R. C. Alencar, J. M. Hickmann, R. Kobayashi, and L. R. P. Kassab, "Femtosecond nonlinear optical properties of tellurite glasses," Appl. Phys. Lett. **89**, 171917 (2006).
91. E. Garmire, "Resonant optical nonlinearities in semiconductors," IEEE J. Sel. Top. Quantum Electron. **6**, 1094–1110 (2000).
92. T. R. Schibli, E. R. Thoen, F. X. Kärtner, and E. P. Ippen, "Suppression of *Q*-switched mode locking and break-up into multiple pulses by inverse saturable absorption," Appl. Phys. B **70**, S41–S49 (2000).
93. R. Wang, B. A. Ruzicka, N. Kumar, M. Z. Bellus, H.-Y. Chiu, and H. Zhao, "Ultrafast and spatially resolved studies of charge carriers in atomically thin molybdenum disulfide," Phys. Rev. B **86**, 045406 (2012).
94. K. Wang, Y. Feng, C. Chang, J. Zhan, C. Wang, Q. Zhao, J. N. Coleman, L. Zhang, W. Blau, and J. Wang, "Broadband ultrafast nonlinear absorption and nonlinear refraction of layered molybdenum dichalcogenide semiconductors," Nanoscale **6**, 10530–10535 (2014).
95. Q. Ouyang, H. Yu, K. Zhang, and Y. Chen, "Saturable absorption and the changeover from saturable absorption to reverse saturable absorption of MoS_2 nanoflake array films," J. Mater. Chem. C **2**, 6319–6325 (2014).
96. P. Y. Yu and M. Cardona, *Fundamentals of Semiconductors: Physics and Materials Properties* (Springer, 2010).
97. S. Kasap, *Principles of Electronic Materials and Devices* (McGraw-Hill, 2005).
98. C. B. Roxlo, M. Daage, A. F. Rupper, and R. R. Chianelli, "Optical absorption and catalytic activity of molybdenum sulfide edge surfaces," J. Catal. **100**, 176–184 (1986).
99. C. B. Roxlo, M. Daage, D. P. Leta, K. S. Liang, S. Rice, A. F. Ruppert, and R. R. Chianelli, "Catalytic defects at molybdenum disulfide "edge" planes," Solid State Ionics **22**, 97–104 (1986).
100. C. B. Roxlo, "Bulk and surface optical absorption in molybdenum disulfide," J. Vac. Sci. Technol. A **5**, 555–557 (1987).
101. X. Yin, Z. Ye, D. A. Chenet, Y. Ye, K. O'Brien, J. C. Hone, and X. Zhang, "Edge nonlinear optics on a MoS_2 atomic monolayer," Science Mag. **344**(6183), 488–490 (2014).
102. M. I. Demchuk, N. V. Kuleshov, and V. P. Mikhailov, "Saturable absorbers based on impurity and defect centers in crystals," IEEE J. Quantum Electron. **30**, 2120–2126 (1994).
103. Z. Zhang, L. Qian, D. Fan, and X. Deng, "Gallium arsenide: a new material to accomplish passively mode-locked Nd:YAG laser," Appl. Phys. Lett. **60**, 419 (1992).
104. M. E. Fermann and I. Hartl, "Ultrafast fibre lasers," Nat. Photonics **7**, 868–874 (2013).
105. A. K. M. Newaz, D. Prasai, J. I. Ziegler, D. Caudel, S. Robinson, R. F. Haglund, Jr., and K. I. Bolotin, "Electrical control of

optical properties of monolayer MoS_2," Solid State Commun. **155**, 49–52 (2013).
106. Z. Yin, H. Li, L. Jiang, Y. Shi, Y. Sun, G. Lu, Q. Zhang, X. Chen, and H. Zhang, "Single-layer MoS_2 phototransistors," ACS Nano **6**, 74–80 (2012).
107. D.-S. Tsai, K.-K. Liu, D.-H. Lien, M.-L. Tsai, C.-F. Kang, C.-A. Lin, L.-J. Li, and J.-H. He, "Few-layer MoS_2 with high broadband photogain and fast optical switching for use in harsh environments," ACS Nano **7**, 3905–3911 (2013).
108. M. Bernardi, M. Palummo, and J. C. Grossman, "Extraordinary sunlight absorption and one nanometer thick photovoltaics using two-dimensional monolayer materials," Nano Lett. **13**, 3664–3670 (2013).
109. M.-L. Tsai, S.-H. Su, J.-K. Chang, D.-S. Tsai, C.-H. Chen, C.-I. Wu, L.-J. Li, L.-J. Chen, and J.-H. He, "Monolayer MoS_2 heterojunction solar cells," ACS Nano **8**, 8317–8322 (2014).
110. L. M. Malard, T. V. Alencar, A. P. M. Barboza, K. F. Mak, and A. M. de Paula, "Observation of intense second harmonic generation from MoS_2 atomic crystals," Phys. Rev. B **87**, 201401(R) (2013).
111. K. F. Mak, K. He, J. Shan, and T. F. Heinz, "Control of valley polarization in monolayer MoS_2 by optical helicity," Nat. Nanotechnol. **7**, 494–498 (2012).
112. H. Zeng, J. Dai, W. Yao, D. Xiao, and X. Cui, "Valley polarization in MoS_2 monolayers by optical pumping," Nat. Nanotechnol. **7**, 490–493 (2012).
113. T. Cao, G. Wang, W. Han, H. Ye, C. Zhu, J. Shi, Q. Niu, P. Tan, E. Wang, B. Liu, and J. Feng, "Valley-selective circular dichroism of monolayer molybdenum disulphide," Nat. Commun. **3**, 887 (2012).
114. H. J. Conley, B. Wang, J. I. Ziegler, R. F. Haglund, S. T. Pantelides, and K. I. Bolotin, "Bandgap engineering of strained monolayer and bilayer MoS_2," Nano Lett. **13**, 3626 (2013).
115. K. Roy, M. Padmanabhan, S. Goswami, T. P. Sai, G. Ramalingam, S. Raghavan, and A. Ghosh, "Graphene-MoS_2 hybrid structures for multifunctional photoresponsive memory devices," Nat. Nanotechnol. **8**, 826–830 (2013).
116. W. Zhang, C.-P. Chuu, J.-K. Huang, C.-H. Chen, M.-L. Tsai, Y.-H. Chang, C.-T. Liang, Y.-Z. Chen, Y.-L. Chueh, J.-H. He, M.-Y. Chou, and L.-J. Li, "Ultrahigh-gain photodetectors based on atomically thin graphene-MoS_2 heterostructures," Sci. Rep. **4**, 3826 (2014).
117. G. Eda and S. A. Maier, "Two-dimensional crystals: managing light for optoelectronics," ACS Nano **7**, 5660–5665 (2013).
118. N. Huo, J. Kang, Z. Wei, S.-S. Li, J. Li, and S.-H. Wei, "Novel and enhanced optoelectronic performances of multilayer MoS_2WS_2 heterostructure transistors," Adv. Funct. Mater. **24**, 7025–7031 (2014).
119. H. Wang, F. Liu, W. Fu, Z. Fang, W. Zhou, and Z. Liu, "Two-dimensional heterostructures: fabrication, characterization, and application," Nanoscale **6**, 12250–12272 (2014).
120. Y. Y. Wang, F. Couny, P. S. Light, B. J. Mangan, and F. Benabid, "Compact and portable multiline UV and visible Raman lasers in hydrogen-filled HC-PCF," Opt. Lett. **35**, 1127–1129 (2010).
121. D. J. Richardson, J. Nilsson, and W. A. Clarkson, "High power fiber lasers: current status and future perspectives," J. Opt. Soc. Am. B **27**, B63–B92 (2010).
122. B. Ortaç, M. Baumgartl, J. Limpert, and A. Tünnermann, "Approaching microjoule-level pulse energy with mode-locked femtosecond fiber lasers," Opt. Lett. **34**, 1585–1587 (2009).
123. W. Renninger, A. Chong, and F. Wise, "Giant-chirp oscillators for short-pulse fiber amplifiers," Opt. Lett. **33**, 3025–3027 (2008).
124. R. I. Woodward, E. J. R. Kelleher, T. H. Runcorn, S. Loranger, D. Popa, V. J. Wittwer, A. C. Ferrari, S. V. Popov, R. Kashyap, and J. R. Taylor, "Fiber grating compression of giant-chirped nanosecond pulses from an ultra-long nanotube mode-locked fiber laser," Opt. Lett. **40**, 387–390 (2015).
125. A. Giesen and J. Speiser, "Fifteen years of work on thin-disk lasers: results and scaling laws," IEEE J. Sel. Top. Quantum Electron. **13**, 598–609 (2007).
126. K. Wu, X. Zhang, J. Wang, X. Li, and J. Chen, "WS_2 as a saturable absorber for ultrafast photonic applications of mode-locked and *Q*-switched lasers," arXiv:1411.5777 (2014).
127. S. H. Kassani, R. Khazaeizhad, H. Jeong, D.-I. Yeom, and K. Oh, "All-fiber Er-doped *Q*-switched laser based on tungsten disulfide saturable absorber," Opt. Mater. Express **5**, 373–379 (2015).
128. D. Mao, Y. Wang, C. Ma, L. Han, B. Jiang, X. Gan, S. Hua, W. Zhang, T. Mei, and J. Zhao, "WS_2 mode-locked ultrafast fiber laser," Sci. Rep. **5**, 7965 (2015).
129. P. Yan, A. Liu, Y. Chen, H. Chen, S. Ruan, S. Chen, I. L. Li, H. Yang, J. Hu, and G. Cao, "Microfiber-based WS_2-film saturable absorber for ultra-fast photonics," Opt. Mater. Express **5**, 479–489 (2015).